LASER-INDUCED BREAKDOWN SPECTROSCOPY (LIBS) FOR INVESTIGATING SURFICIAL CONDENSATION OF SEMI-VOLATILES ON VOLCANIC SPATTER

A FINAL REPORT SUBMITTED TO THE DEPARTMENT OF GEOLOGY AND GEOPHYSICS, UNIVERSITY OF HAWAI'I AT MĀNOA, IN PARTIAL FULFILLMENT OF THE REQUIREMENTS FOR THE DEGREE OF

MASTER OF SCIENCE
IN
GEOLOGY AND GEOPHYSICS

APRIL 2020

BY
OLLIANDER BEUCLER

COMMITTEE:
JASPER KONTER (CHAIR)
AARON PIETRUSZKA
THOMAS SHEA

Abstract

Magmatic volatiles impact volcanic eruption dynamics: a volatile-rich magma has a higher potential for an explosive eruption than a volatile-poor (degassed) magma. At depth and high pressure, volatiles remain in solution, or dissolved within the magma. As magma rises, the decrease in pressure results in volatiles exsolving from bulk magma into a vapor phase. The presence of semi-volatile metals can be used to understand degassing at depth and provide evidence for magmatic processes. The objective of this study is to generate elemental profiles using a Laser-Induced Breakdown Spectroscopy (LIBS) technique for Kīlauea spatter samples and investigate if semi-volatile metals are enriched on the spatter surfaces. In this study, a range of elements (Li, Cu, Na, Zn, Cr, Tl, Pd, Ni, Ba, Mn, B, and Ti), including four that are semi-volatile (Li, Cu, Na, Zn), were analyzed. Increased quantities of analyte volatile elements were observed on the surface relative to the interior of the spatter samples. Other included elements, present in low ratios, demonstrated greater variation throughout the sample. Overall, the data suggests that an estimated ~1% of total semi-volatiles in the gas plume condense on the surface of erupted material. This study demonstrates that a novel LIBS technique can be used to investigate surficial condensation of semi-volatile elements on spatter during a volcanic eruption degassing phase.

Table of Contents

List of Figures and Tables

1. Introduction

Beginning in the early 1800s, the foundation of spectro-chemical analysis was developed as scientists correlated colors of visible light emissions to elements. The development of atomic theory facilitated spectroscopists to recognize that emitted wavelengths are unique to specific atoms and ions. By 1960, the first laser was developed. Work published by Cremers and Radziemski in 1981 paved the way for Laser-Induced Breakdown Spectroscopy (LIBS) in research. Beginning around 1995, publications using LIBS increased in prevalence and continue to increase each year (Cremers et al., 2006).

LIBS is a cost-effective and in-situ analysis method. The instrument uses a lens-focused, pulsed laser to ablate the sample surface and create a temporary plasma. While this is a destructive technique, overall damage can be confined to a small fraction of sample volume. LIBS analysis is used in a dynamic range of studies including planetary research, archaeology to date artifacts, as well as measuring minor and major elements in geologic samples. The LIBS system includes a spectrometer that records wavelengths between 200nm and 850nm, which are specific to ionization states of the elemental composition. The produced spectra within this range includes hundreds of atomic emission lines. The qualitative and quantitative interpretation for the chemical composition is related to the emission peak height as an indication of element abundance in the sample. The National Institute of Standards and Technology (NIST) Atomic Spectra database is used to reference elements for the established wavelengths and observed intensities associated with specific wavelengths.

In this project, we take advantage of the limited ablation depth per individual laser shot. Consequently, LIBS has potential as a depth-profiling analysis technique. The objective of this study was to generate elemental profiles of Puʻu ʻŌʻō and Kīlauea Lower East Rift Zone (LERZ) spatter samples and investigate if semi-volatile elements show compositional enrichments on spatter surfaces. These enrichments would be represented by changes in ratios of the semi-volatile intensities versus low-volatility (refractory) elements, when comparing the surface relative to interior composition

2. Background

2.1. Laser-Induced Breakdown Spectroscopy

As detailed in Cremers et al. (2006), the produced emission spectra from LIBS analysis is limited by a few factors that include matrix effect, self-absorption, and variation with laser spark and the produced plasma. Matrix effects (spectral, physical and chemical) may cause changes to emission intensities when sample properties vary (Hahn and Omenetto 2012). Physical matrix effects are related to sample surface characteristics (vesicle properties, hardness, texture), which can cause variations in how much material is ablated with each laser pulse. Chemical matrix effects occur when the presence of one element alters the emission intensity of another element (Cremers et al., 2006). For instance, two samples containing the same element concentration (12% Mg) may yield different emission spectra for that element, if the samples consist of different overall materials. Spectral matrix effects include the interference of strong emission lines with weaker lines. This issue can be resolved by selecting peaks known to not have interferences during data analysis. Self-absorption may also occur and be reflected in the emission spectra (Lepore, 2017). Self-absorption occurs when the produced plasma contains atoms with conflicting excitation energies. Self-absorbed spectra result in spectral lines with either a dip replacing the element peak or an emission line with a flattened peak (Takahashi and Thornton, 2017). Various statistical techniques have been used in LIBS data analysis to compensate for these effects: multivariate analysis (partial least squares), univariate analysis, or relating the relative ratio of an analyte intensity to a constant element intensity (Eggins, 1998; Clegg et al., 2009; Konter et al., 2019).

2.2. Elemental Distribution During Volcanic Processes

2.2.1. Major Elements

Major elements constitute more than 1 wt.% each of total rock composition. This group of elements is essential for distinguishing physical (density, viscosity) and thermodynamic (phase relations, melting points) properties (Philpotts & Ague, 2013). Effusive eruptions at Hawaiian volcanoes produce basaltic lava. Subsequently, the overall SiO_2 concentration is ~50 wt.% with olivine dominating, and pyroxene and plagioclase feldspar present in minor amounts (Helz, 2014). MgO value range (6.0 to 17.8 wt.%) for bulk rock composition documented in the last 200 years of Kīlauea eruptive history is used to gauge processes such as magma transport, fractional crystallization, and magma mixing occurring in the volcanic plumbing system (Garcia

et al., 1989; Clague et al., 1991; Garcia et al., 2003). Magnesium is also a moderately refractory element (in relation to condensation temperature), and we will use this abundant element in our LIBS analysis.

2.2.2, Volatile Elements

Magmatic gas has an important role in the behavior of a volcanic eruption. The volume of volcanic gas emitted may exceed the volume of volatiles dissolved in the magma (Shinohara, 2008). Excess degassing occurs when the volume of emitted volcanic gas is greater than the volume of volatiles dissolved in the magma (Andres et al. 1991; Wallace, 2001). By this criterion, Hawaiian volcanism does not significantly observe excess degassing, but is commonly observed in Plinian, Strombolian, and Vulcanian eruptions (Wallace 2001; Sharma et al., 2004). As magma rises and produces a gas phase, volatile and semi-volatile trace elements diffuse through the magma and partition into the vapor phase of an eruption. Volatiles in volcanic plumes (H_2O, CO_2, SO_2, etc.) originate from two main sources; volatilization of metals from magma with a gas-particle phase, or from a phase that includes erupted magma fragments and bubbles bursting superficially (Shinohara, 2009). Distinguishing these two pathways is important for understanding the volatilization of elements from the erupted material and subsequent emission of these elements into the environment. One methodology introduced by Rubin (1997) calculates emanation coefficients ($\mathcal{E}_x$) to classify the volatility of elements found within volcanic eruptions.

$$\mathcal{E}_x = \frac{C_i - C_f}{C_i}; where \frac{C_i \; is \; the \; initial \; concentration \; of \; "x" \; element \; in \; the \; magma}{C_f \; is \; the \; final \; concentration \; of \; "x" \; element \; post \; eruption}$$

With this equation, three groups are distinguished: group one volatile metals are $\mathcal{E}_x > 10^{-2}$, group two semi-volatile metals are $\mathcal{E}_x = 10^{-4}$ to 10^{-2}, and group three non-volatile metals are $\mathcal{E}_x < 10^{-4}$. Rubin (1997) discusses the use of highly volatile ^{210}Po and ^{210}Pb as a gauge of degassing processes. The ^{210}Po isotopic disequilibria (with respect to its radioactive parent isotope) due to degassing are also used to obtain an eruption age. In the latter case, it is critical that ^{210}Po measured on magmatic products is not contaminated by condensation of the Po from the eruptive gas phase. In order to investigate effects of condensation, this study focuses on semi-volatile elements due to their greater affinity to condense from the vapor and, therefore, have a greater probability to be preserved on sample surfaces. The following elements are classified as semi-volatile: Cu, Ir, As, Te, Zn, Tl, In, Mo, Sn, W, Sb, Cs, K, Ni, Li, and Na (Mather et al., 2015).

2.3. History of Hawaiian Volcanic Eruptions

Over the past 200 years, Hawaiian volcanic eruptions have been characterized by effusive basaltic lavaerupted in the middle of an oceanic plate. The Hawaiian archipelago includes eight islands (ordered oldest to youngest): Niʻihau, Kauaʻi, Oʻahu, Molokaʻi, Lānaʻi, Kahoʻolawe, Maui, and the Island of Hawaiʻi (Macdonald et al., 1983). The samples for this study were collected on the Island of Hawaiʻi. The Island of Hawaiʻi includes five subaerial volcanoes (ordered oldest to youngest): Kohala, Mauna Kea, Hualālai, Mauna Loa, and Kīlauea (Moore and Clague, 1992), and this study focuses on the Kīlauea volcanic system. Kīlauea volcanism exhibits a tholeiitic shield-building stage with activity occurring between three regions; summit caldera and two rift zones (southwest and east) (Jackson, 1972; Helz et al., 2014).

Puʻu ʻŌʻō, a cone located on Kīlauea east rift zone, hosted one of the longest sustained eruptions (about thirty-five years occurring from 1983 to 2018) with an erupted volume estimated about 4.4 km3 (USGS 2019). Throughout Puʻu ʻŌʻō eruptive history, systematic isotopic variations distinguish lavas from summit erupted lavas (Greene et al., 2013). Given the Kīlauea plumbing system is well constrained, these isotopic variations can be traced with $^{206}Pb/^{204}Pb$ variations in lavas from the summit and rift zones to trace mantle heterogeneities (Pietruszka, et al., 2018). Mantle heterogeneities imprint the composition of the parental magma delivered to the volcano, and thus, potentially influence temporal and spatial extent of magmatic degassing (Wallace and Anderson, 2000). Highly volatile elements degas closest to the summit: semi-volatile elements predominately exsolve as magma travels into rift zones (Schmincke, 2004).

On April 30, 2018, the collapse of Puʻu ʻŌʻō vent initiated the largest LERZ eruption and caldera collapse in the documented eruptions from the last two hundred years (Neal et al., 2018). The 2018 Kīlauea eruption is also credited as one of the most well-documented eruptions to date. Observations and data collected from the eruption have produced insights into lesser understood volcanic processes: caldera collapse, small and explosive basaltic eruptions, degassing processes, and magma transport mechanisms (Gansecki et al., 2019). In total, the LERZ fissures extended about 6.8 km and covered about 35.5 km^2 with twenty-four of the total 24 fissures opening by May 3, 2018. Early erupted magma had a ≤5 wt.% MgO and may have evolved from the 1955 magma through fractional crystallization. Given the proximity and similarities in composition, the magma supply was potentially stored in LERZ since 1955. Activity continued until August 4,

2018. Figure 1 (left) is an overview of Kīlauea with the location of samples included in this study labeled. The map on the right (USGS) depicts a Lava Flow Thickness map for the 2018 LERZ eruption. By late May, much of the 2018 eruption activity occurred at fissure eight with effusion rates between 50 to 200 m^3/s and fountain heights up to 80 m (Neal et al., 2018).

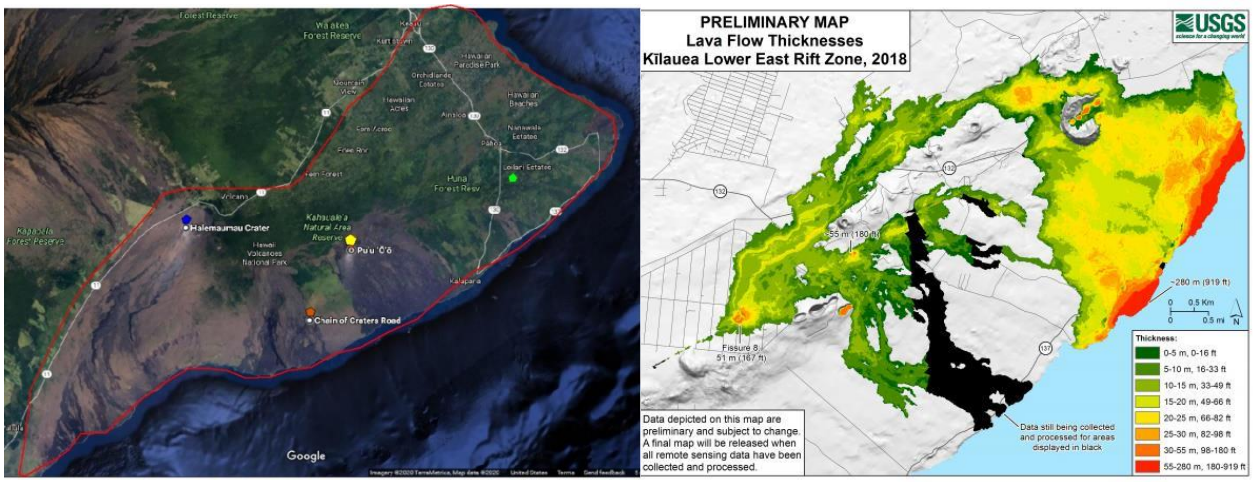

Figure 1: (Left) Labeled Google Map image of Kīlauea [Blue: summit location, Red: Chain of Craters Road, Yellow: Pu'u 'Ō'ō vent, Green: Fissure Eight located in the LERZ]; (Right) Preliminary Map of Lava Flow Thickness for the 2018 LERZ eruption (USGS).

3. Methods

3.1. Background About Samples

Samples were collected from Kīlauea LERZ and Pu'u 'Ō'ō eruptive activity. Samples were collected along Chain of Craters Road (Flat Spatter sample), Pu'u 'Ō'ō (last gasp of activity), and Fissure Eight during the 2018 eruption. A standard glass sample (D15-19), previously cut, was included as a baseline. The samples were brought to the University of Hawai'i at Manoa for glass analysis with a Laser-Induced Breakdown Spectroscopy (LIBS) instrument.

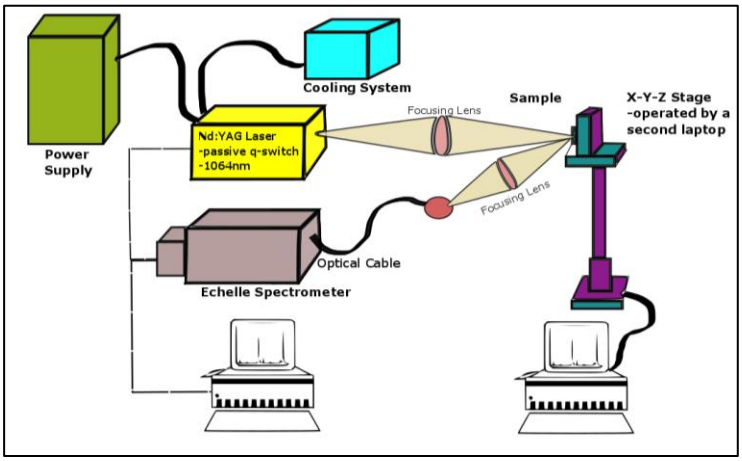

Figure 2: Inkscape Diagram of LIBS setup

3.2. Instrumentation

The layout of the LIBS system is shown in Figure 2. The laser used in this analysis is a Q-switched Nd-YAG laser with an output of 20mJ per pulse. It operates at ~15Hz (pulses/s) with a pulse length of approximately 6 nanoseconds. Spectral emissions were collected with an Echelle type spectrometer; Catalina scientific EMU- 60/120 with LX cassette and a resolution of ~60,000. To generate element profiles with sufficient signal, comparing surface composition to interior composition, a pre-programmed X-Y-Z stage was devised from a repurposed Computer Numerical Control (CNC) milling machine. The stage was used to ablate spots on the sample surface in an eleven by eleven grid to generate the spectral measurement at a specific depth, and successive layers of sample were ablated to create the profile. Figure 3a depicts the stage that was controlled with a second computer and repeated for up to fifteen rounds (layers).

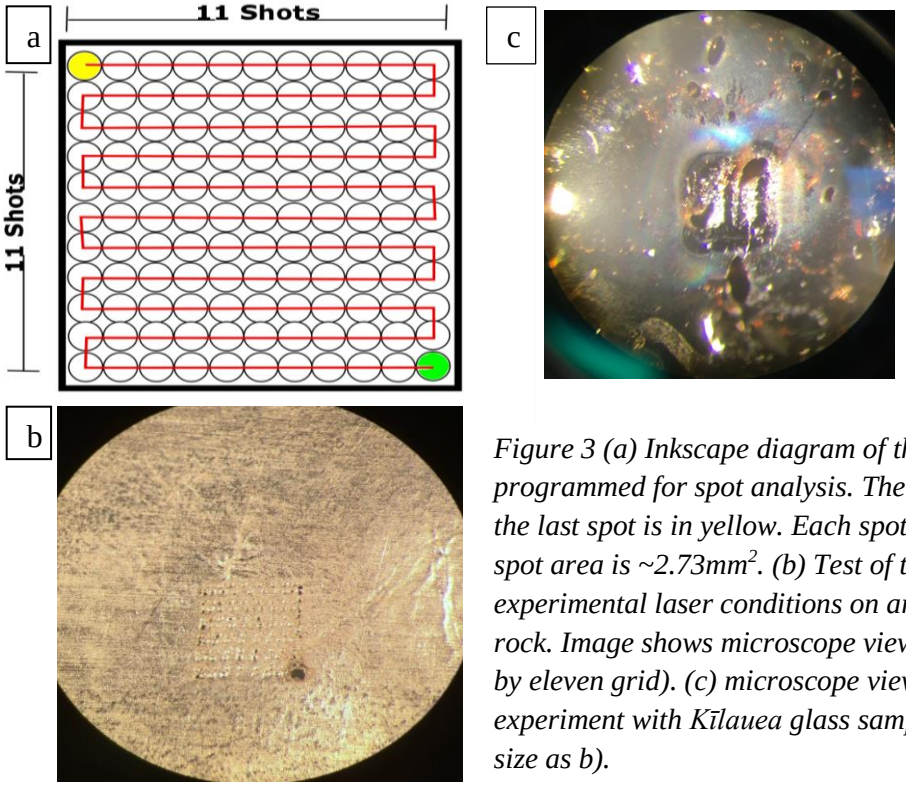

Figure 3 (a) Inkscape diagram of the X-Y-Z stage sequence programmed for spot analysis. The first spot is in green and the last spot is in yellow. Each spot is ~150μm, total 11x11 spot area is ~2.73mm^2. (b) Test of the X-Y-Z stage setup using experimental laser conditions on an aluminum foil wrapped rock. Image shows microscope view after one round (eleven by eleven grid). (c) microscope view of result of full experiment with Kīlauea glass sample (excavated pit same size as b).

4. Results

4.1. Initial Assessment

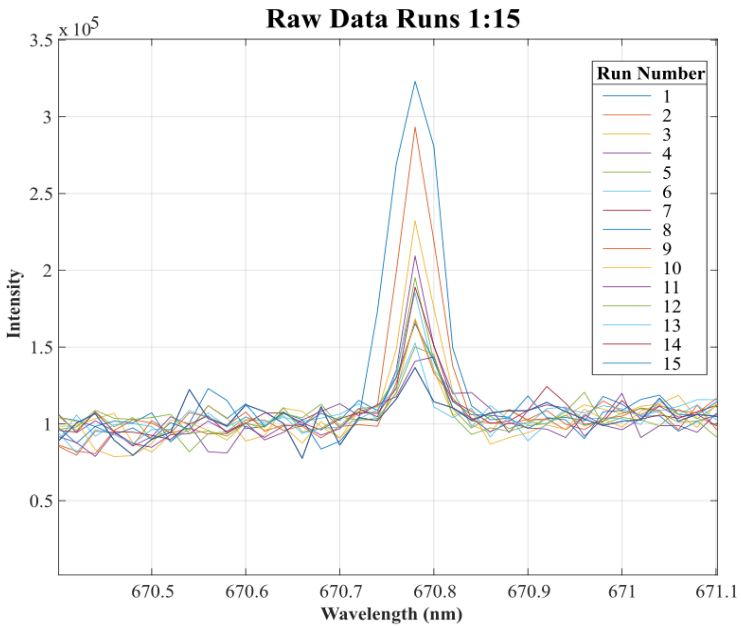

Figure 4: Flat Spatter Data runs 1:15 for Li: 670.8nm

Analyzed samples were initially reviewed by overlapping the difference of raw data to identify the presence of trends. The project explored which elements (if any) were present in ratios inconsistent with the interior sample composition. This rapid analysis technique calculates relative intensities for analyte elements by eliminating spectral variations in an element present at a constant concentration. Figure 4 depicts an example of a peak at 670.8nm (Li) demonstrating a trend where, as the laser ablated the sample, the intensity decreased sequentially. Figure 5 plots sample *Flat Spatter* raw spectral emission data from 200nm to 850nm as the relationship of run number to the difference in intensity of interior to surface [Run(1:15) minus Run(15)]. The figure combines all spectral emission data to indicate differences in emission intensities from the sequential runs relative to the intensities associated with the interior (run fifteen or last run). Differences between surface and interior intensities are less significant after the fifth run. Figure 5 demonstrates the presence of a trend and was used as a baseline for further investigation. For comparison, the other samples were processed similarly. These figures are included in the appendix: A (Fig. 9), B (Fig. 11), C (Fig. 13), and D (Fig. 15).

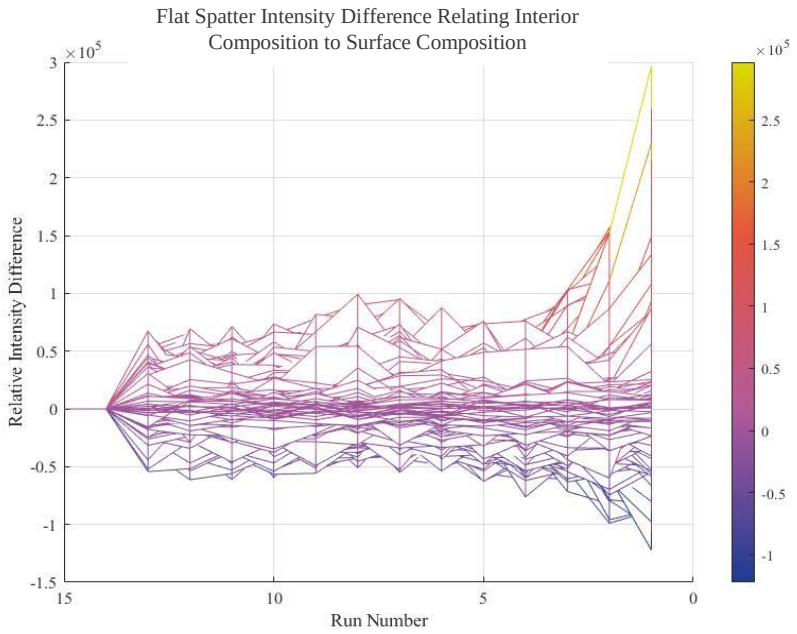

Figure 5: Flat Spatter sample intensity difference of Run(1:15) – Run (15) The left side depicts spectral emissions for the interior: the right depicts spectral emissions for the surface. A positive difference or (colors within the upper-color-bar-range) signifies spectral emissions present in a higher intensity than the interior. A negative difference or (colors within the lower-color-bar-range) signifies spectral emissions present in a lower intensity than the interior.

4.2. Percent Ratios of Elements Present

For the uses of this study, elements were portrayed as percent ratios relative to magnesium, an element known and verified with this data to yield the same intensity from the sample surface to interior i.e. :

$$\frac{\left[\frac{volatile\ element\ "n"}{Mg}\right]_{surface}}{\left[\frac{volatile\ element\ "n"}{Mg}\right]_{interior}} * 100\%$$

This approach minimized variations in elemental peak intensity attributed to laser power (or laser-sample coupling) fluctuation and followed the suggested notation for an enrichment factor (e.g., Mather, 2015). Within a gas plume setting, this calculated enrichment factor correlates the presence of volatiles to refractory elements as compared to related, degassing lava (e.g., Mather, 2015). Prior investigations into Puʻu ʻŌʻō and Kīlauea volatile geochemistry were used as a baseline to identify a range of elements known or potentially present. Based on the volatility classification using emanation coefficients (Ɛx) as presented by Rubin (1997), at least one

element from the three groups (volatile, semi-volatile, and low to non-volatile) was included. The following elements were plotted as a percent ratio relative to magnesium intensity; Li, Cu, Na, Zn, Cr, Tl, Pd, Ni, Ba, Mn, B, and Ti. Elements Li, Cu, Na, Zn, Tl, Pd, and Ni are in the semi-volatile group. Boron is classified as a volatile element. The remaining elements, Ba, Ti, Mn, and Cr, are low to non-volatile elements. The NIST database was referenced to identify the above elements of interest based on wavelength data. Appendix A, Figure 8, includes graphs A through D for standard *D15-19*. This sample was included because it provided results on a previously cut sample of volcanic glass, allowing for an evaluation of repeated ablation effects with no potential surface condensates (effectively, a baseline sample). Appendix B, Figure 10, includes graphs A through L for the *Flat Spatter* sample. Appendix C, Figure 12, includes graphs A through L for the *Pu'u 'Ō'ō sample*. Appendix D, Figure 14, includes graphs A through L for the *Fissure 8 Kīlauea sample*.

Results of the different element groups can be summarized as showing a potential surface condensation signal only for the semi-volatile elements. The volatile element B does not show the same surface enrichment trends, likely resulting from the higher volatility preventing condensation under the eruptive conditions. Similarly, refractory elements do not show strong signals either, likely related to these elements remaining mostly in the magma. Therefore, the semi-volatile elements present the most significant results.

The results overall showed between 45% and 160% increase in volatile content on sample surfaces for semi-volatile elements Li, Cu, Na, and Zn. Values were provided in Table 1 (and derived from Appendix A-D, Fig. 8, 10, 12, 14), and showed the highest values for Li and Cu. The minimum values for the ratios shown, together with the 2 standard deviations calculated for the innermost 4 depth layers in each sample, provided an estimate of the variability with the LIBS method to estimate ratios. Therefore, for most elements, the ratios needed to be at least 10-20% higher from the interior, preferably for more than one layer, to be statistically different than the interior. The elements listed in Table 1 best meet this requirement.

Table 1: Comparison of Four Samples; Minimum Percentage, Maximum Percentage*, and Two Standard Deviation Percentage for Analyte Elements*

**: percent ratio of analyte relative to Mg*

Element		Standard D15-19	Flat Spatter	Pu‘u ‘Ō‘ō	Fissure Eight Kīlauea
Li	Min (%)	94.8	90.7	88.6	81.8
	Max (%)	138.7	220.5	185.5	192.7
	[100+2*stdev%] baseline (±)	7.26	27.2	16.9	25.3
Na	Min (%)	97.4	97.1	88.6	92.2
	Max (%)	108.4	118.2	201.6	145.4
	[100+2*stdev%] baseline (±)	3.74	4.11	20.7	16.2
Cu	Min (%)	94.4	94.2	90.6	80.0
	Max (%)	118.1	238.3	169.9	246.3
	[100+2*stdev%] baseline (±)	8.65	16.5	12.7	27.6
Zn	Min (%)	95.8	92.6	89.8	88.5
	Max (%)	111.1	129.3	151.6	129.3
	[100+2*stdev%] baseline (±)	4.34	12.2	21.8	18.7

5. Discussion

5.1. Interpretation of Baseline Sample

Glass sample *D15-19* functioned as a baseline sample to establish if the elements with surface composition trends in excess of two standard deviations were an artifact of elemental fractionation during laser ablation or present from eruptive processes. It is well-established that laser-ablation sampling of silicate minerals removes analytes of different volatility at different rates. However, when ablated pit diameter significantly exceeds total analyzed depth, this error is minimized (e.g., Eggins et al., 1998). As one location was ablated tens to hundreds of times, this process (down-hole fractionation; Mukherjee et al., 2019) results in the ratio of volatile versus refractory elements to artificially increase incrementally through the course of data collection (Eggins et al., 1998). As related to this study, data collected was spread over a large enough area to minimize down-hole fractionation effects as depth increases. A study with a comparable Nd:YAG laser specification, Eggins et al. (1998) measured a ~20% change in $^{209}Bi/^{232}Th$ ratio attributed to down-hole fractionation effects. Our study ablated ~15 shots, which is equivalent to 15% of Eggins et al. (1998) total analyzed depth. Hence, the expected variation from down-hole fractionation should be minimal (~3% ratio change). Observations from baseline sample, *Standard D15-19,* showed changes in analyte volatile to refractory element ratios lacking down-hole fractionation effects (Appendix A, Fig. 8). Instead, majority analyte elements demonstrated elevated ratios at the sample surface and with decreased ratios at the interior. Comparing the overall shape of these figures, the standard sample *D15-19* had a decreasing, nearly linear slope as run number (or depth) increased. Figure 7 compares percent ratio versus run number for four elements (Li, Cu, Na, and Zn) between three true surface samples and the baseline. These elements were present at ratios in higher than 100%, but lower and with less variation than the true surface sample. For the interests of this study, elements present in ratios in excess of the standard and with greater variation are significant. As discussed further below, true sample surfaces (*Flat Spatter, Puʻu ʻŌʻō, Kīlauea Fissure 8*) showed statistically significant trends for several elements, and therefore, both baseline and true samples were fitted with a logarithmic curve to compare relative behavior. A logarithmic curve was the best fit for data that rapidly decreased then leveled out.

5.2. Interpretation of Kīlauea Samples

Data for the true samples from Kīlauea showed statistically significant changes in their volatile versus refractory element ratios. In particular, the sample from location one, *Flat Spatter*, suggests a higher difference in surface to interior composition with an exponential decline by the fifth depth layer and minimal variation thereafter (Appendix B, Fig. 10, 11). The change implies a significantly higher volatile content at the surface. The sample from Puʻu ʻŌʻō more closely parallels the shape of standard sample *D15-19*, although the *Puʻu ʻŌʻō* sample has a higher slope and initial intensity. This suggests that the surface variation was less than variation observed within the *Flat Spatter* sample (Appendix C, Fig. 12, 13).

5.3. Percent Ratio of Volatile Elements to Magnesium

In contrast to the linear increase in volatile to refractory element ratios reported by Eggins et al. (1998), the analyte volatile elements in this study were strongly correlated with a logarithmic function (correlation coefficient *r* exceeds 0.6). The strongest effects were observed for Li, Cu, Na, and Zn (Table 1, Fig. 7), which were all part of the semi-volatile group of elements specifically targeted. Other elements in the same group had spectral intensities with less than 10% variation, which signifies these elements are inadequate for quantification. However, the four elements with well-defined spectral emissions showed statistically significant increases for this group. When trends of these elements were compared between samples and the baseline, true-surface samples had both higher values at the surface and a steeper slope increase. Both *Flat Spatter* sample and *Kīlauea Fissure Eight* sample could not be measure adequately for elements Tl, Ni, Ba, Ti and Mn. For both samples these elements demonstrate a lower analyte/Mg ratio in the exterior layers. These elements did not display a similar relationship for the *Puʻu ʻŌʻō* sample.

The values recorded (up to 260%) for the semi-volatile elements (Li, Cu, Na, and Zn) can be compared to previously reported quantities in degassing lavas. For example, Gauthier et al. (2016) (represented in fig. 6) reported values for semi-volatile elements at the lava surface for up to 100 times the value in the gas plume for Kīlauea, Erta Ale, and Holuhraun. The samples analyzed in this study, have experienced condensation of the semi-volatile metals on the spatter surface. Hence, these samples amount to approximately twice the ratio observed in the melt.

Consequently, it appears a very small fraction of the semi-volatile elements condense on such surfaces. This implies that semi-volatile and volatile metals will be transported over larger distances than the immediate area impacted by pyroclastic material. Also, as demonstrated in the *Flat Spatter* data, Cu is present at a higher enrichment factor than Zn and Tl. This suggests that in the gas plume more volatile elements (represented on the right side of fig. 6) have a higher affinity to remain in the gas phase. In a cooling gas plume, Cu, the least volatile element included in this data set, theoretically would condense first, while more volatile elements will not condense until the temperature decreases. As a result, Cu should be present at a higher ratio on the surface. Furthermore, highly volatile elements such as ^{210}Po and ^{210}Pb (used to investigate timescales of magmatic processes) should not be significantly impacted by these condensation process, as the error level of the U-series disequilibria measurements for Po and Pb are of similar or larger magnitude (e.g., Rubin et al., 1994).

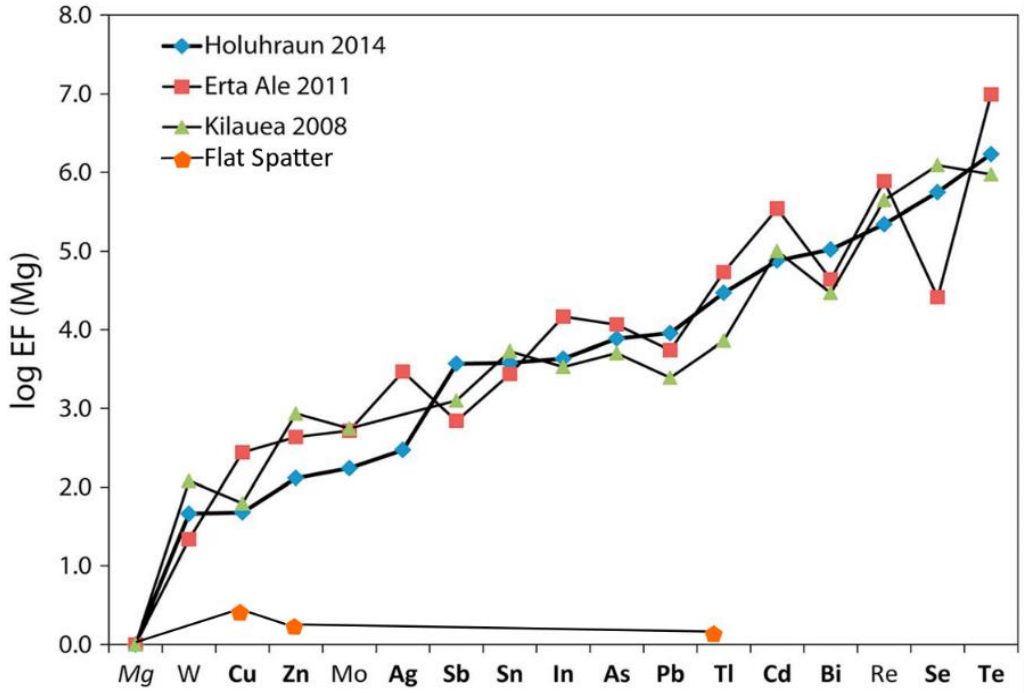

Figure 6: Element volatility represented as Enrichment Factors relative to Mg. The included elements are ordered by increasing volatility. Data collected from Flat Spatter sample is included for comparison with three other data. Elements included represent reliable data.

[Data collected for Holuhraun 2014 , Erta Ale 2011, Kīlauea 2008 from Gauthier et al. (2016), Mather et al. (2012) and Zelenski et al., (2013)]

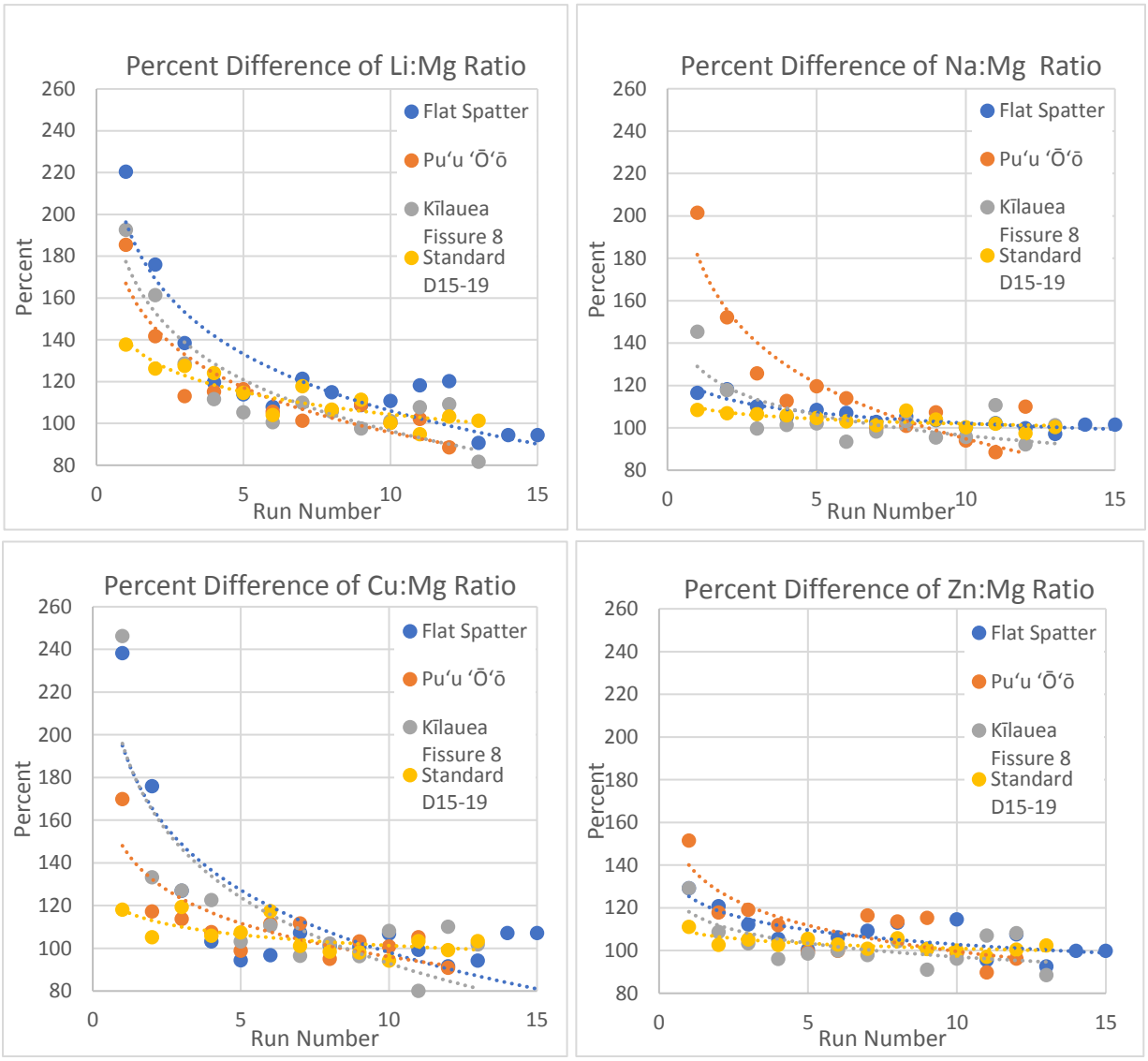

Figure 7: Li, Cu, Na, and Zn Ratios observed for our three true-surface Kīlauea samples and standard sample D15-19 as a baseline. Logarithmic line of best fit included as a dashed line for each sample

6. Conclusion

In order to evaluate the condensation of volatile materials on volcanic spatter surfaces through degassing, we investigated three Kīlauea samples with a novel use of LIBS. The included samples: *Flat Spatter* from Chain of Craters Road, *Pu'u 'Ō'ō* from the Pu'u 'Ō'ō vent in the last gasp of activity, and a sample from Fissure Eight located on Kīlauea LERZ). The data demonstrated that our samples from Kīlauea displayed increased quantities of volatile elements on the surface relative to interior composition: Li, Cu, Na, and Zn. These elements provide a gauge of how semi-volatile metals behave, and therefore provide guidance an upper bound on condensation from eruptive gases for highly volatile metals. Highly volatile elements such as ^{210}Po and ^{210}Pb can be used for quantifying degassing processes, and the disequilibria of ^{210}Po that are generated during degassing can be used for dating eruptions. However, ^{210}Po produced during the degassing phase will artificially inflate the abundance of ^{210}Po on sample surfaces, if it condenses and is then analyzed as part of the magma fraction. To best constrain effects of condensation, semi-volatile elements suit the needs of this study because this group of elements have a higher affinity to condense on the sample surface and subsequently have a higher probability for observation. The data were quantified as enrichment factors or percent ratios relative to magnesium. In constraining potential errors, sample *D15-19* served as a baseline to identify if trends (including an excess of two standard deviations) of analyte to refractory element ratios occurred as a result of eruptive processes, or as an artifact of elemental fractionation during laser ablation. The results suggest about ~1% of semi-volatile elements in the gas plume may condense on erupted pyroclastic materials. The data also demonstrated that some element ratios were not significantly variable to establish a strongly correlated trend between the sample surface to interior composition. Hence, this study supports the idea that the LIBS technique is useful for investigating surficial condensation of semi-volatile elements during a degassing phase of volcanic eruptions.

7. Works Cited

Andres, R. J., W. I. Rose, P. R. Kyle, S. de Silva, P. Francis, M. Gardeweg, and H. Moreno Roa (1991), Excessive sulfur dioxide emissions from Chilean volcanoes, J. Volcanol. Geotherm. Res., 46, 323 – 329, doi:10.1016/0377-0273(91)90091-D

Clague, D. A., Weber, W. S. & Dixon, J. E., (1991). Picritic glasses from Hawaii. Mature 353, 553-556.

Clegg, S.M., Sklute, E., Dyar, M.D. "Multivariate Analysis of Remote Laser-Induced Breakdown Spectroscopy Spectra Using Partial Least Squares, Principal Component Analysis, and Related Techniques". Spectrochim. Acta, Part B. (2009). 64(1): 79–88.

Cremers, David A., and Leon J. Radziemski. "Handbook of Laser-Induced Breakdown Spectroscopy." (2006), doi:10.1002/0470093013.

Eggins, S.M., Rudnick, R.L. and Mcdonough, W.F. (1998). The composition of peridotites and their minerals: a laser-ablation ICP-MS study. *Earth and Planetary Science Letters 154: 53-71.*

Gansecki, Cheryl & Lee, R. & Shea, Thomas & Lundblad, Steven & Hon, Ken & Parcheta, Carolyn. (2019). The tangled tale of Kīlauea's 2018 eruption as told by geochemical monitoring. Science. 366. eaaz0147. 10.1126/science.aaz0147.

Garcia, M., Ho, R., Rhodes, J. *et al.* Petrologic constraints on rift-zone processes. *Bull Volcanol* **52,** 81–96 (1989). https://doi.org/10.1007/BF00301548

Garcia, M.O., (2003). A Petrologic Perspective of Kilauea Volcano's Summit Magma Reservoir. J. Petrol. 44, 2313–2339. doi:10.1093/petrology/egg079

Gauthier, P.-J., Sigmarsson, O., Gouhier, M., Haddadi, B., and Moune, S. (2016), Elevated gas flux and trace metal degassing from the 2014–2015 fissure eruption at the Bárðarbunga volcanic system, Iceland, J. Geophys. Res. Solid Earth, 121, 1610– 1630, doi:10.1002/2015JB012111.

Greene, A. R., Garcia, M. O., Pietruszka, A. J., Weis, D., Marske, J. P., Vollinger, M. J. & Eiler, J. (2013). Temporal geochemical variations in lavas from Kı¯lauea's Pu'u 'O 'o eruption (1983-2010): cyclic variations from melting of source heterogeneities. Geochemistry, Geophysics, Geosystems 14, 4849–4873.

Hahn, D. W., & Omenetto, N. (2012). *Laser-Induced Breakdown Spectroscopy (LIBS), Part II: Review of Instrumental and Methodological Approaches to Material Analysis and Applications to Different Fields. Applied Spectroscopy, 66(4), 347–419.* doi:10.1366/11-06574

Helz, Rosalind T., et al. "Petrologic Insights into Basaltic Volcanism at Historically Active Hawaiian Volcanoes." *Professional Paper*, (2014), pp. 237–292., doi:10.3133/pp18016.

Jackson, E. D., Silver, E. A. & Dalrymple, G. B. Hawaiian-Emperor chain and its relation to Cenozoic circumpacific tectonics, (1972). Geol. Soc. Am. Bull. 83, 601–618

Lepore, K.H., Fassett, C.I., Breves, E.A. "Matrix Effects in Quantitative Analysis of Laser-Induced Breakdown Spectroscopy (LIBS) of Rock Powders Doped with Cr, Mn, Ni, Zn, and Co". Appl. Spectrosc. (2017). 71(4): 600–626

Macdonald, G.A., Abbott, A.T. and Peterson, F.L., (1983). Volcanoes in the Sea: The Geology of Hawaii, 2nd edition. University of Hawaii Press.

Mather, Tamsin A. "Volcanoes and the Environment: Lessons for Understanding Earth's Past and Future from Studies of Present-Day Volcanic Emissions." (2015) *Journal of Volcanology and Geothermal Research*, vol. 304 pp. 160–179., doi:10.1016/j.jvolgeores.2015.08.016.

Mather, T. A., et al. (2012), Halogens and trace metal emissions from the on-going 2008 summit eruption of Kīlauea volcano, Hawai'i, *Geochim. Cosmochim. Acta*, 83, 292–323, doi:10.1016/j.gca.2011.11.029.

Matthias Geissbuehler (2020). Colormaps compatible with red-green color perception deficiencies (https://www.mathworks.com/matlabcentral/fileexchange/31761-colormaps-compatible-with-red-green-color-perception-deficiencies), MATLAB Central File Exchange.

Moore, J.G. and Clague, D.A., (1992). Volcano Growth and Evolution of the Island of Hawaii. GSA Bulletin, 104(11): p. 1471-1484. doi: 10.1130/0016-7606(1992).

Mukherjee, P.K., Souders, A.K., Sylvester, P.J., (2019). Accuracy and precision of U–Pb zircon geochronology at high spatial resolution (7–20 μm spots) by laser ablation-ICP-single-collector-sector-field-mass spectrometry. J. Anal. At. Spectrom. 34, 180–192. doi:10.1039/C8JA00321A

Neal, C. A., Brantley, S. R., Antolik, L., Babb, J., Burgess, M., Calles, K., Desmither, L. (2018). *The 2018 rift eruption and summit collapse of Kīlauea Volcano. Science, eaav7046.* doi:10.1126/science.aav7046

Philpotts, Anthony R., and Jay J. Ague. *Principles of Igneous and Metamorphic Petrology*. Cambridge University Press, 2013.

Pietruszka, A.J., Marske, J.P., Heaton, D.E., Garcia, M.O., Rhodes, J.M., (2018). An Isotopic Perspective into the Magmatic Evolution and Architecture of the Rift Zones of Kīlauea Volcano. J. Petrol. 59, 2311–2352. doi:10.1093/petrology/egy098

Rubin, K. (1997). *Degassing of metals and metalloids from erupting seamount and mid-ocean ridge volcanoes: Observations and predictions.* Geochimica et Cosmochimica Acta, 61(17), 3525–3542. doi:10.1016/s0016-7037(97)00179-8

Rubin, K.H., Macdougall, J.D., Perfit, M.R., (1994). 210Po–210Pb dating of recent volcanic eruptions on the sea floor. Nature 368, 841–844. doi:10.1038/368841a0

Schmincke, H.-U. Volcanism. Springer, 2004.

Sharma, K., S. Blake, S. Self, and A. J. Krueger (2004), SO2 emissions from basaltic eruptions, and the excess sulfur issue, Geophys. Res. Lett., 31, L13612, doi:10.1029/2004GL019688

Shinohara, H. (2008). *Excess degassing from volcanoes and its role on eruptive and intrusive activity. Reviews of Geophysics, 46(4).* doi:10.1029/2007rg000244 .

Takahashi, Tomoko, and Blair Thornton. "Quantitative Methods for Compensation of Matrix Effects and Self-Absorption in Laser Induced Breakdown Spectroscopy Signals of Solids." (2017) *Spectrochimica Acta Part B: Atomic Spectroscopy*, Elsevier.

U.S. Geological Survey. *Volcano Hazards Program HVO Kīlauea*. 19 June 2019, volcanoes.usgs.gov/volcanoes/Kīlauea/geo_hist_1983.html.

Wallace, P. and Anderson, A.T, (2000). *Volatiles in Magmas*. Encyclopedia of Volcanoes, Academic Press, p.149-170

Wallace, P. J. (2001), Volcanic SO2 emissions and the abundance and distribution of exsolved gas in magma bodies, J. Volcanol. Geotherm. Res., 108, 85 – 106, doi:10.1016/S0377-0273(00)00279-1.

Zelenski, M. E., T. P. Fischer, J. M. de Moor, B. Marty, L. Zimmermann, D. Ayalew, A. N. Nekrasov, and V. K. Karandashev (2013), Trace elements in the gas emissions from the Erta-Ale volcano, Afar, Ethiopia, *Chem. Geol.*, *357*, 95–116, doi:10.1016/j.chemgeo.2013.08.022.

Appendix A

Figure 8 : Standard D15-19: Graphs A: D

The dots plotted represent element (n) plotted as a percent ratio relative to Mg. Red lines represent (±) two standard deviations (in percent) to represent the expected variation of the analyte within the sample and are centered on a grey dotted line that represents 100%. Data plotted outside of this range represents statistically significant data. Left-most x-axis represents the surface composition right-most represents interior composition

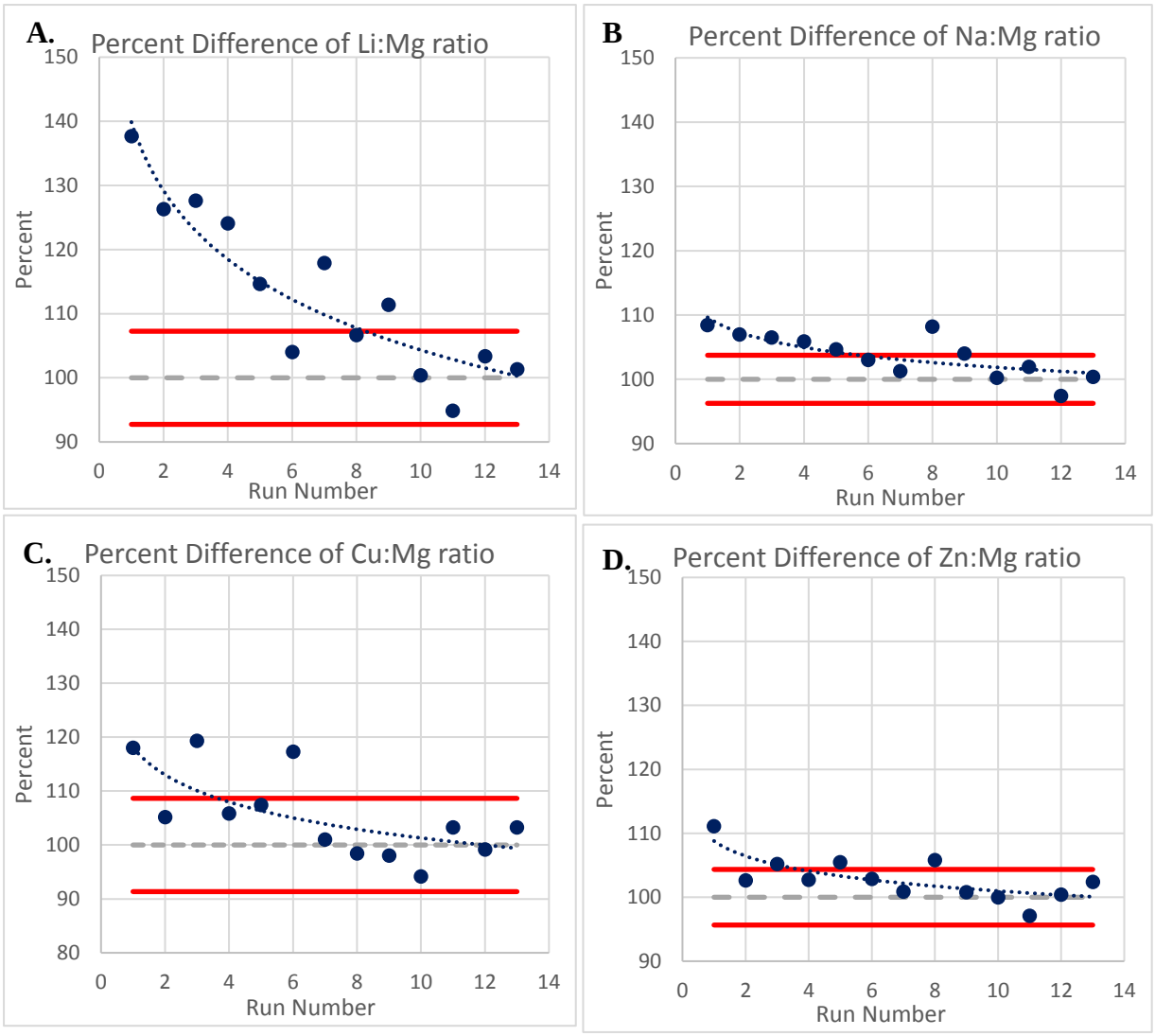

Appendix A

Figure 9: Standard D15-19

Figure produced in MatLab plots run number for interior (left) to surface (right) versus "relative intensity difference" as a relationship of Run(1:15) – Run (15). The color bar on the right characterizes the magnitude of intensity difference. For a small group of wavelengths, there appear to be groups of increasing and decreasing intensities; while, majority wavelengths remain constant. This sample represents a baseline for the three true-surface Kīlauea spatter samples.

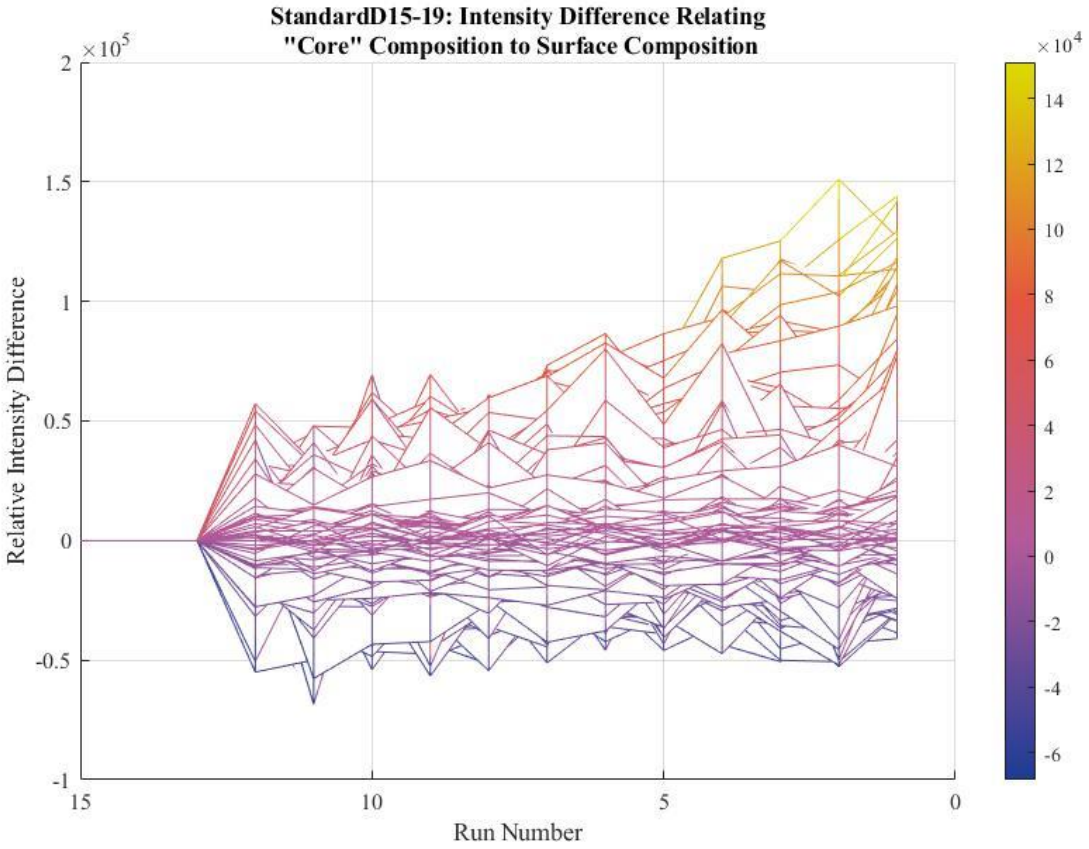

Appendix B

Figure 10: Flat Spatter Sample; Graphs A: L
Same as figure 8 for Flat Spatter sample

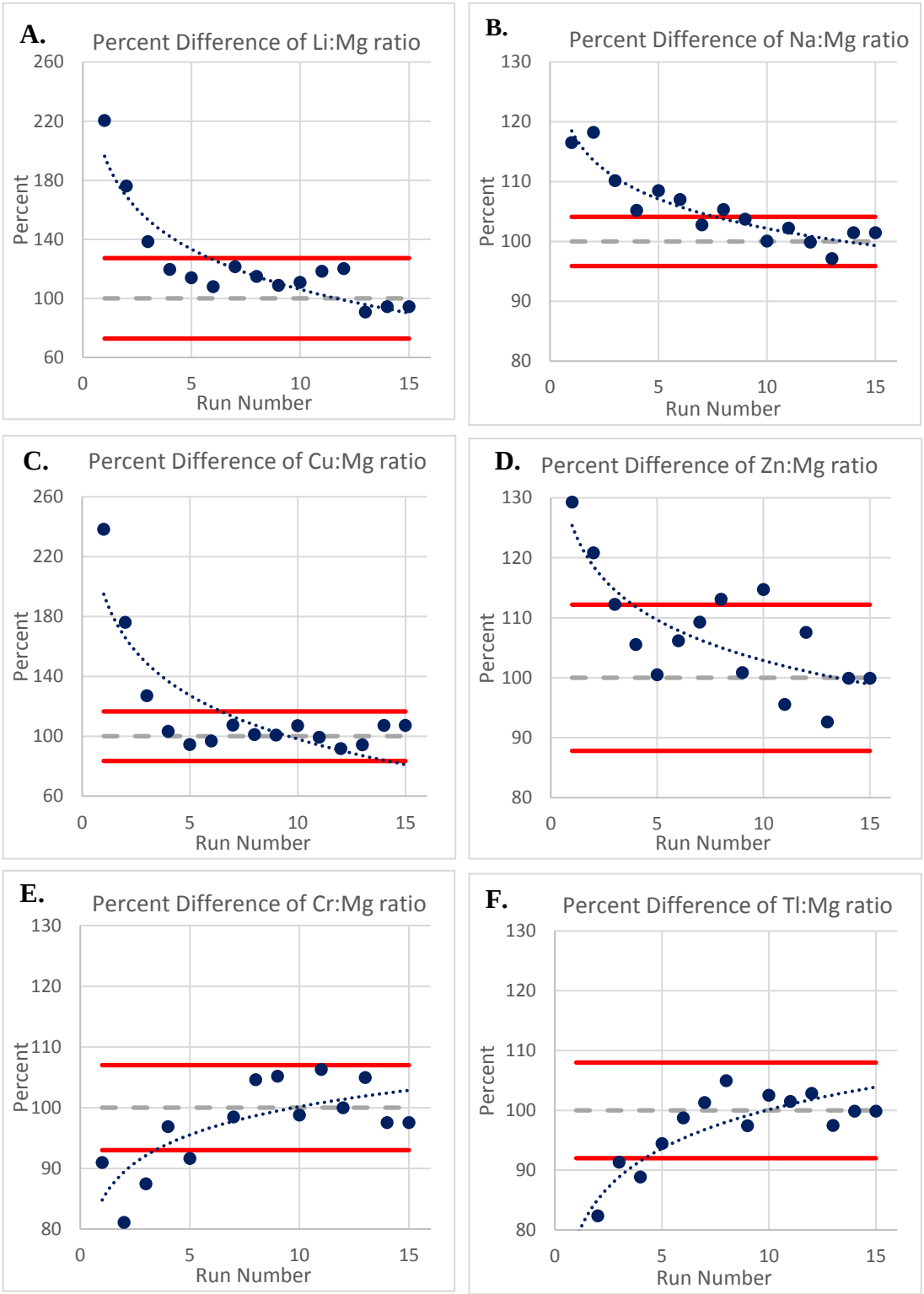

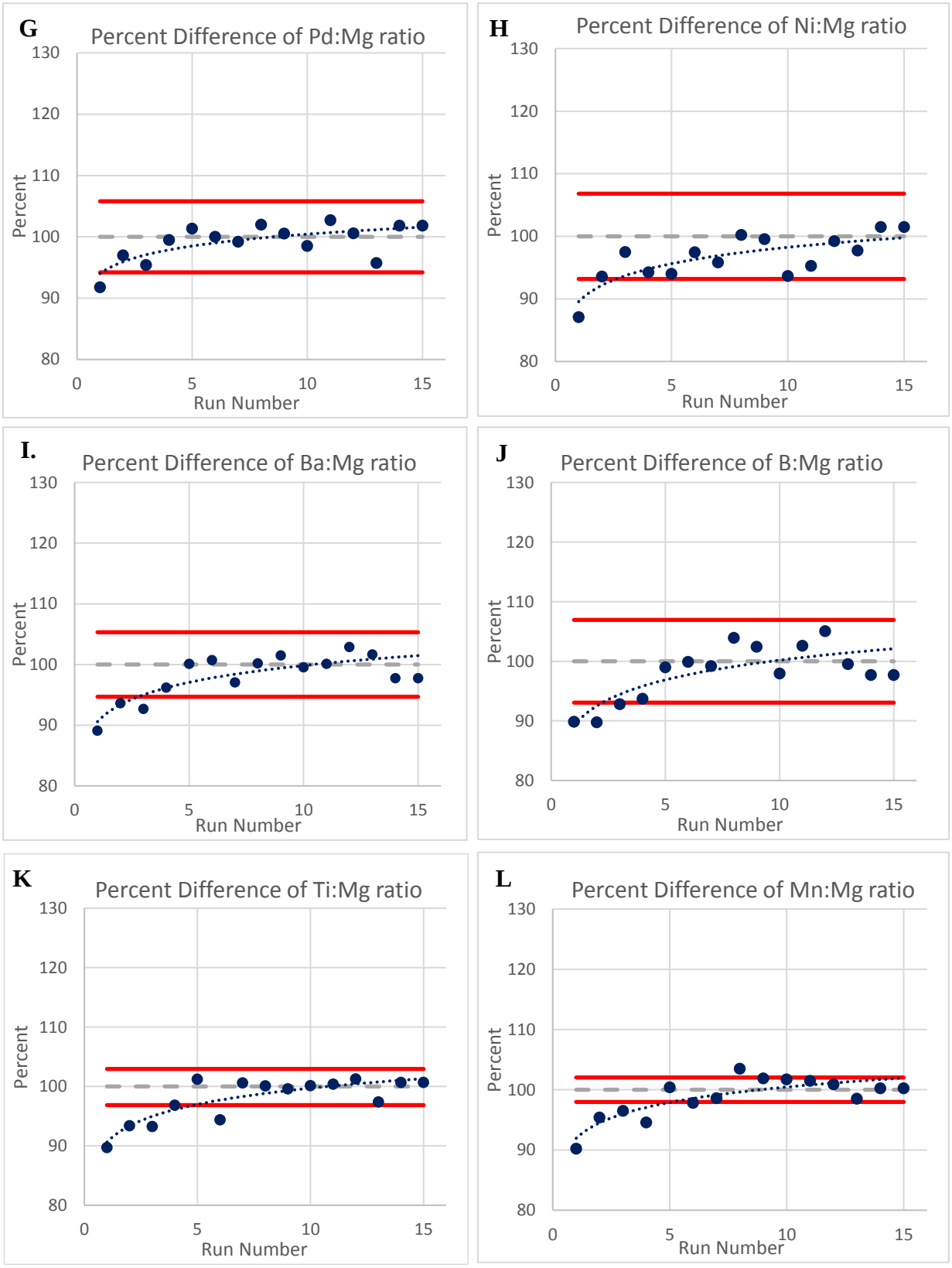
G
Percent Difference of Pd:Mg ratio
H
Percent Difference of Ni:Mg ratio
I.
Percent Difference of Ba:Mg ratio
J
Percent Difference of B:Mg ratio
K
Percent Difference of Ti:Mg ratio
L
Percent Difference of Mn:Mg ratio
Percent
Run Number
130
120
110
100
90
80
0
5
10
15

Appendix B

Figure 11 : Flat Spatter Sample; Location 1, 2

Same as figure 9 for Flat Spatter sample; data based on location one. Other locations evaluated similarly for consistency

Location 1:

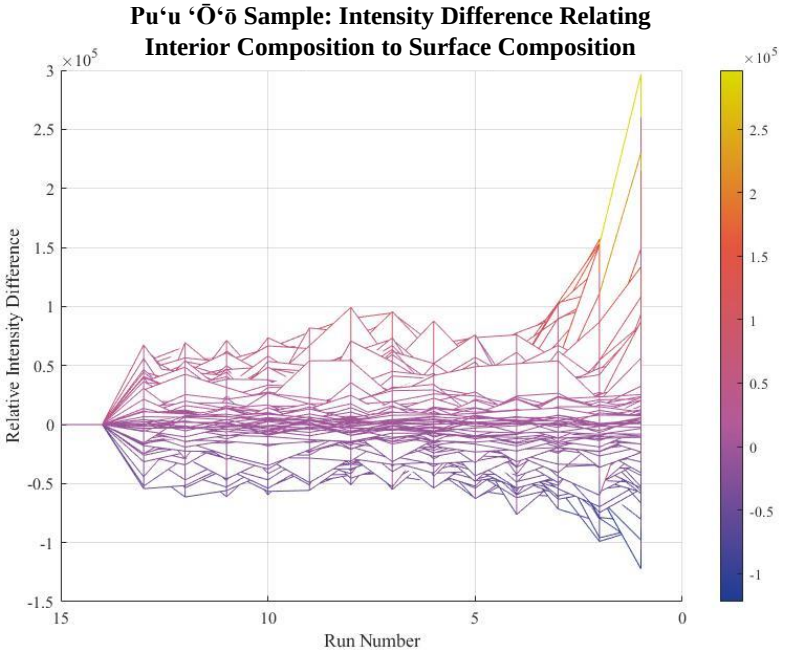

Location 2:

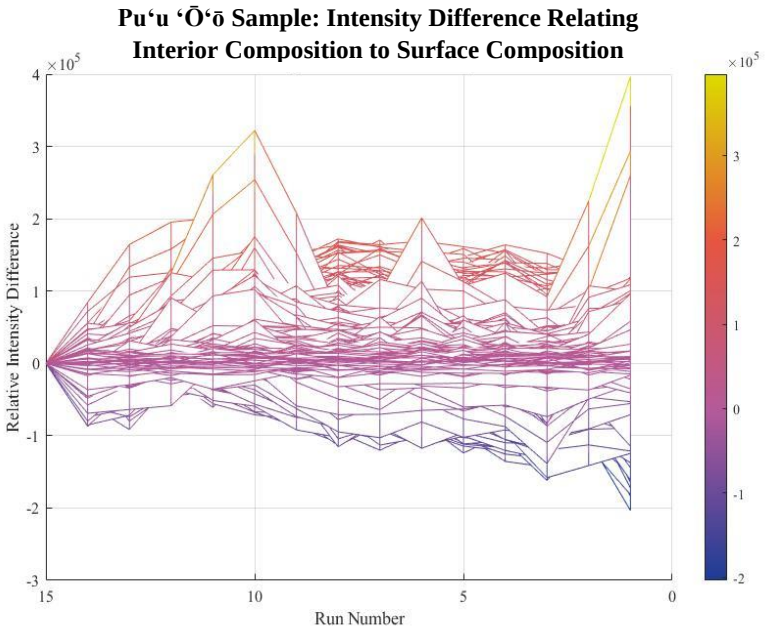

Appendix C

Figure 12: Pu‘u ‘Ō‘ō sample; Graphs A: L
Same as figure 8 for Pu‘u ‘Ō‘ō sample

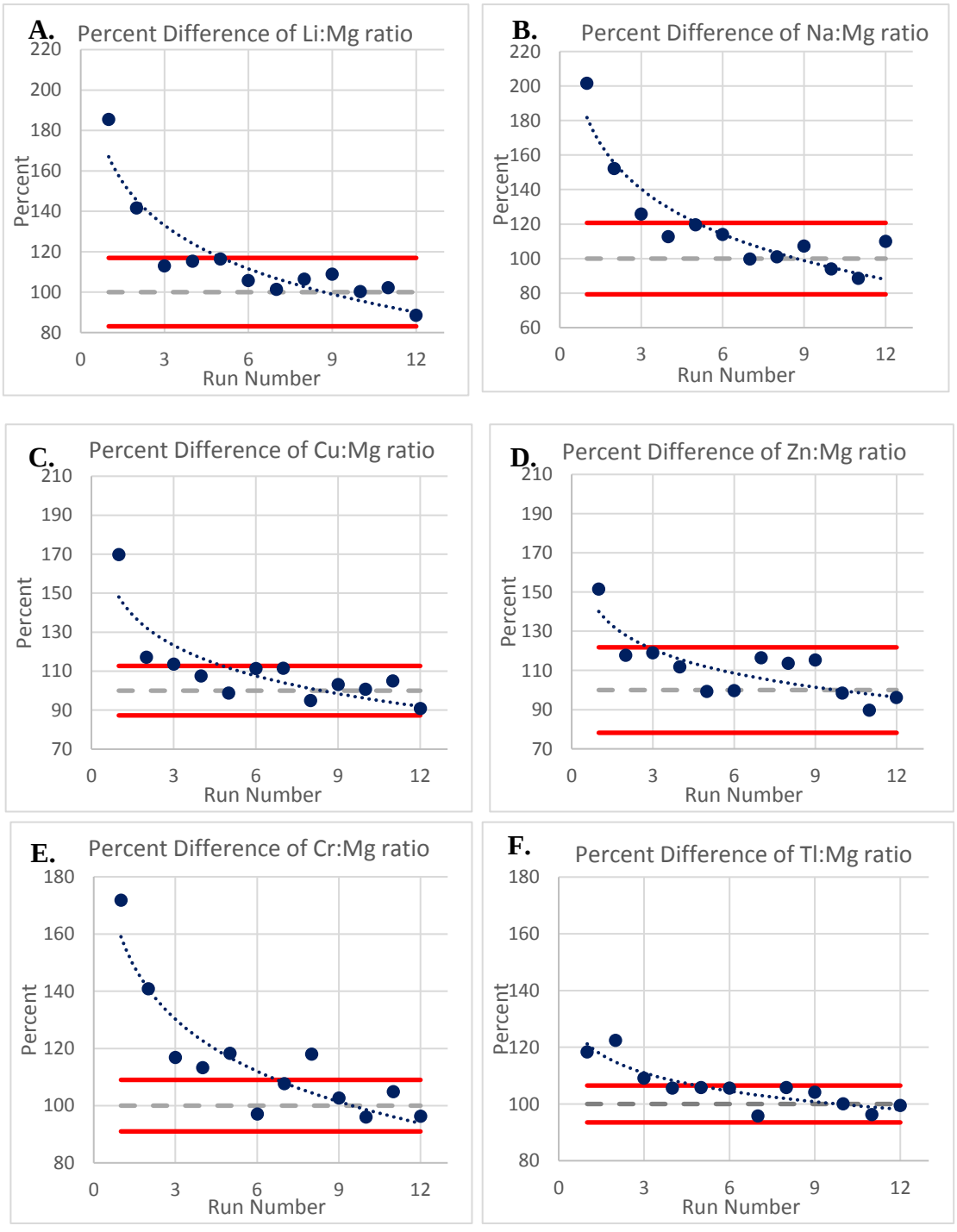

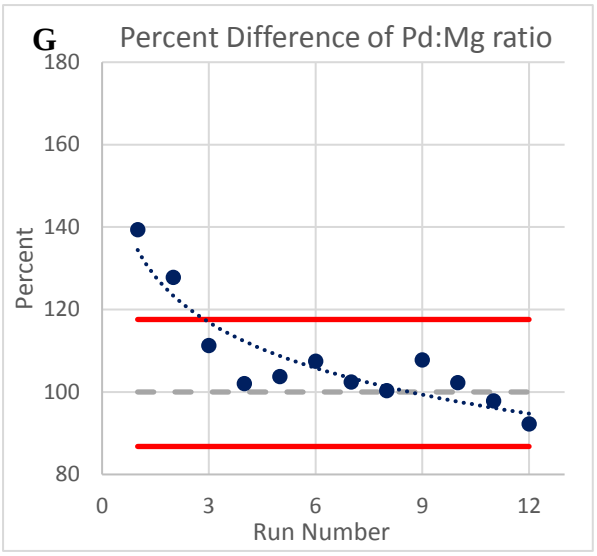
G
Percent Difference of Pd:Mg ratio
Percent
Run Number
180
160
140
120
100
80
0
3
6
9
12

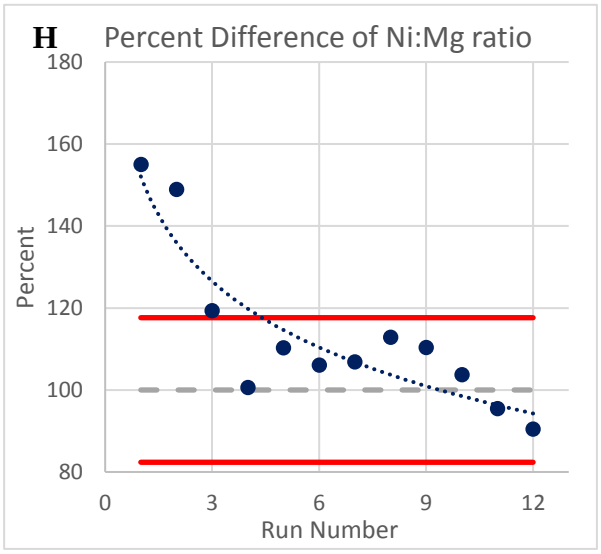
H
Percent Difference of Ni:Mg ratio
Percent
Run Number
180
160
140
120
100
80
0
3
6
9
12

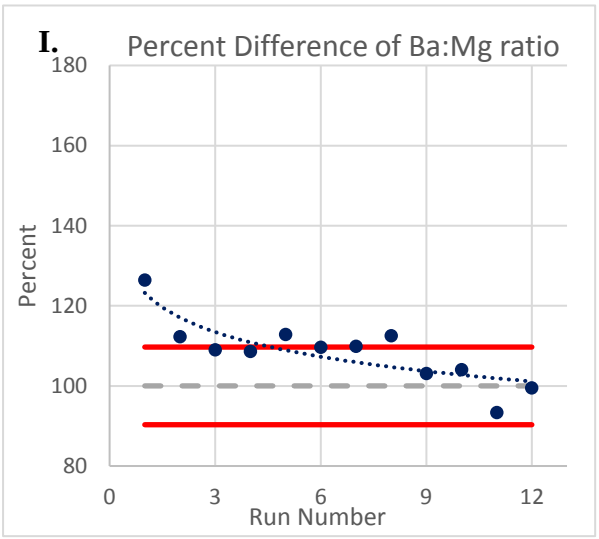
I.
Percent Difference of Ba:Mg ratio
Percent
Run Number
180
160
140
120
100
80
0
3
6
9
12

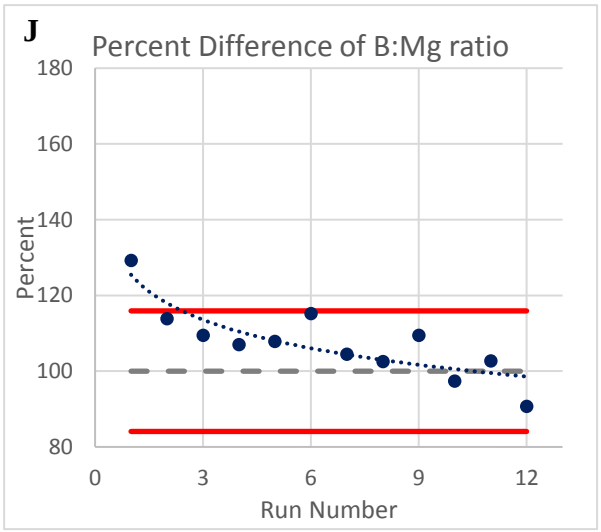
J
Percent Difference of B:Mg ratio
Percent
Run Number
180
160
140
120
100
80
0
3
6
9
12

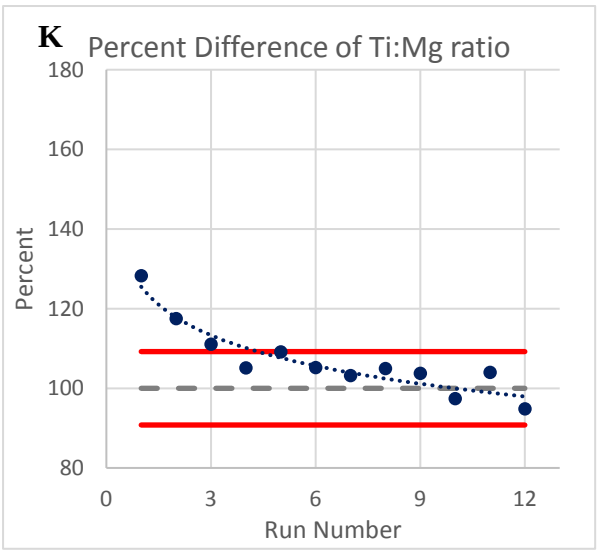
K
Percent Difference of Ti:Mg ratio
Percent
Run Number
180
160
140
120
100
80
0
3
6
9
12

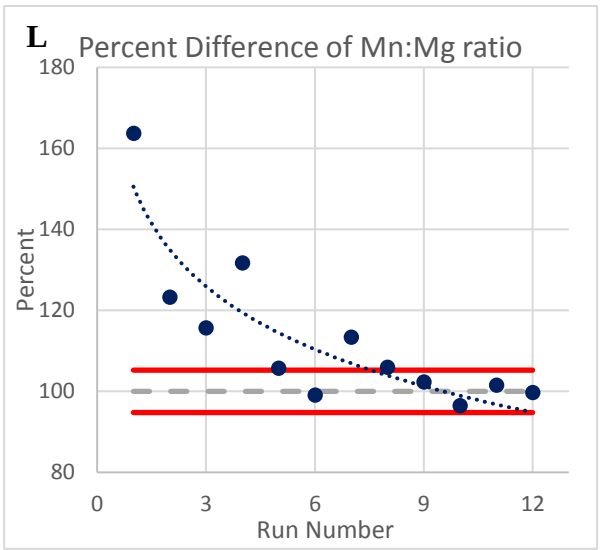
L
Percent Difference of Mn:Mg ratio
Percent
Run Number
180
160
140
120
100
80
0
3
6
9
12

Appendix C:

Figure 13: Pu‘u ‘Ō‘ō sample; Intensity Difference relating Interior to Surface composition
Same as figure 9 for Pu‘u ‘Ō‘ō sample

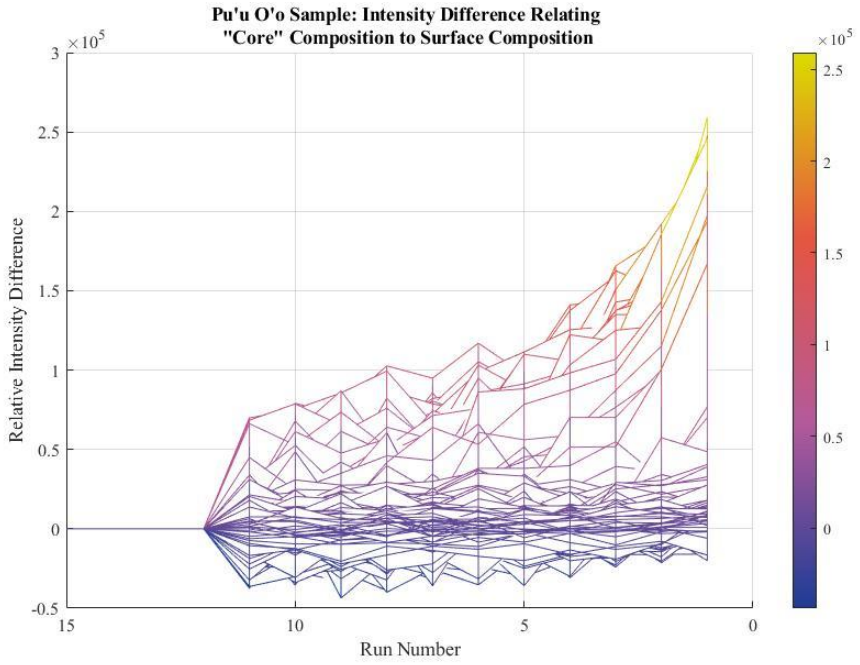

Appendix D

Figure 14: Kīlauea Fissure Eight sample; Graphs A: L

Same as figure 8 for Kīlauea sample

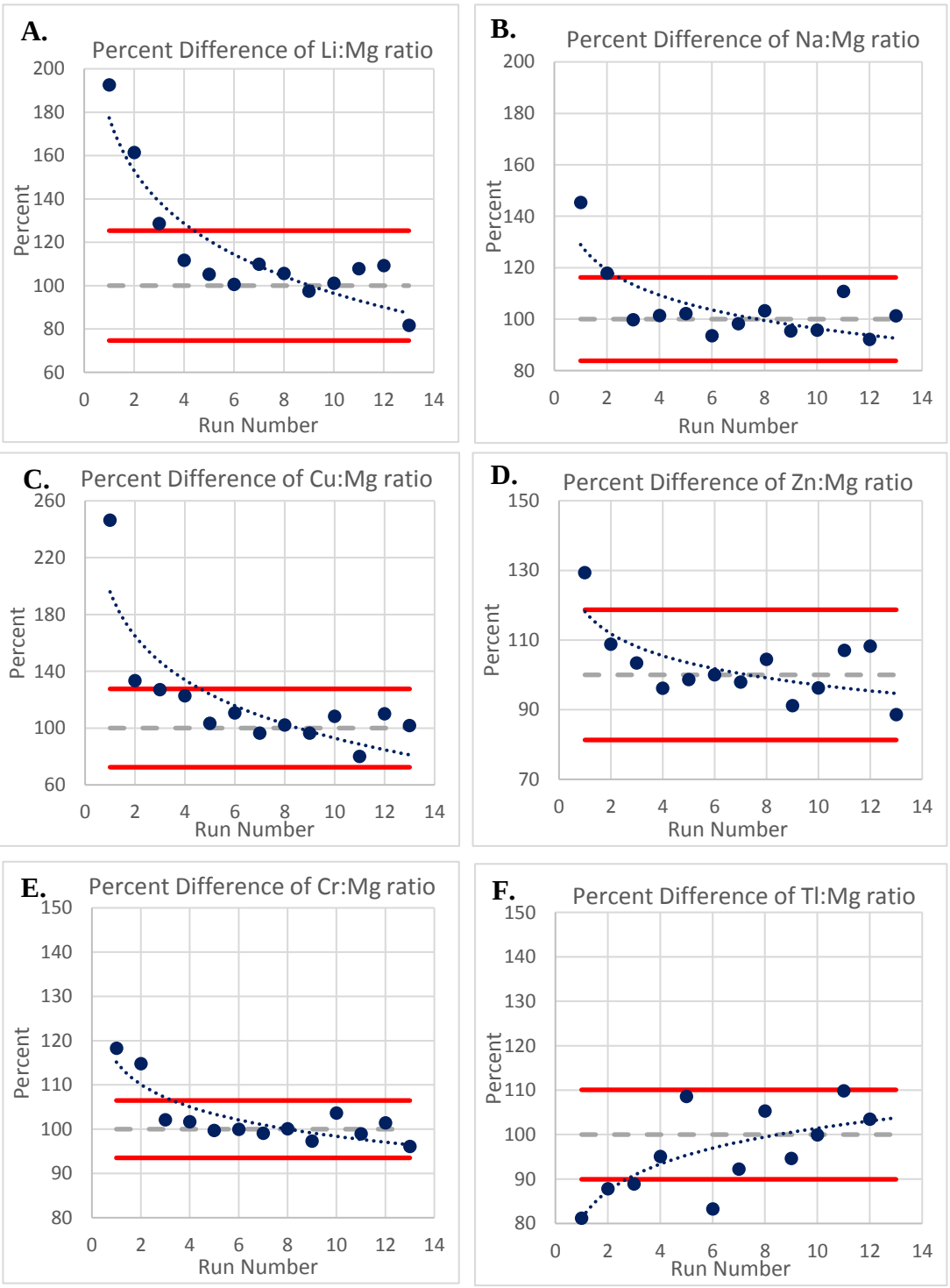

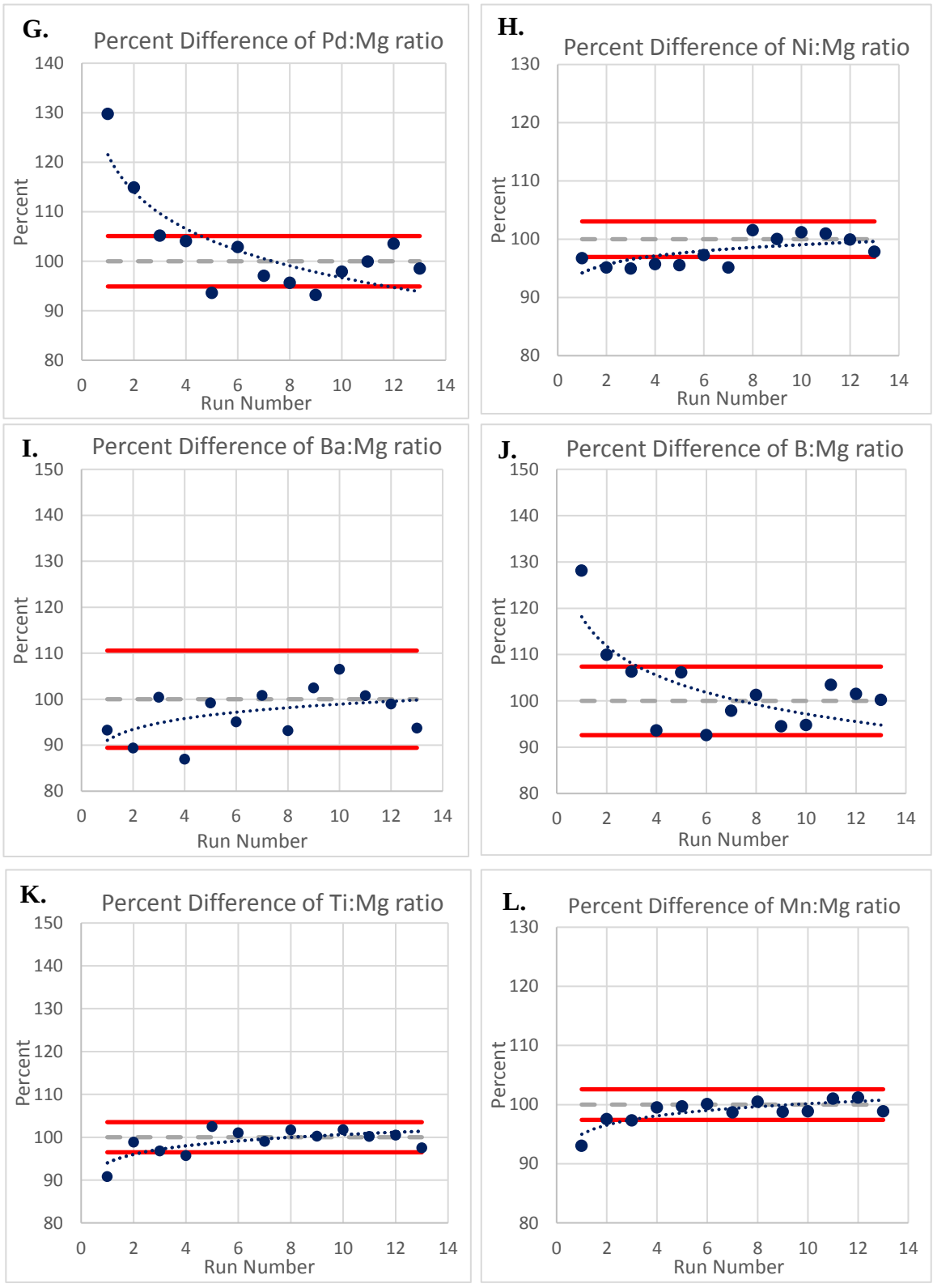
G.
Percent Difference of Pd:Mg ratio
Percent
Run Number
H.
Percent Difference of Ni:Mg ratio
Percent
Run Number
I.
Percent Difference of Ba:Mg ratio
Percent
Run Number
J.
Percent Difference of B:Mg ratio
Percent
Run Number
K.
Percent Difference of Ti:Mg ratio
Percent
Run Number
L.
Percent Difference of Mn:Mg ratio
Percent
Run Number

Appendix D: Figure 15
Kīlauea Fissure Eight sample; Intensity Difference relating Interior to Surface composition in Graphs A:D

Same as figure 9 for Kīlauea Fissure Eight. Sample data was based on location one (v1). Other locations evaluated similarly for consistency